Acta Mechanica Sinica
DOI 10.1007/s10409-013-0041-2

RESEARCH PAPER

Pressure-sensitive plasticity of lithiated silicon in Li-ion batteries

Ke-Jie Zhao · Yong-Gang Li · Laurence Brassart

Received: 30 March 2013 / Revised: 10 May 2013 / Accepted: 23 May 2013

Abstract Lithiation-induced plasticity is a key factor that enables Si electrodes to maintain long cycle life in Li-ion batteries. We study the plasticity of various lithiated silicon phases based on first-principles calculations and identify the linear dependence of the equivalent yield stress on the hydrostatic pressure. Such dependence may cause the compression-tension asymmetry in an amorphous Si thin film electrode from a lithiation to delithiation cycle, and leads to subsequent ratcheting of the electrode after cyclic lithiation. We propose a yield criterion of amorphous lithiated silicon that includes the effects of the hydrostatic stress and the lithiation reaction. We further examine the microscopic mechanism of deformation in lithiated silicon under mechanical load, which is attributed to the flow-defects mediated local bond switching and cavitation. Hydrostatic compression confines the flow defects thus effectively strengthens the amorphous structure, and vice versa.

The project was supported by the National Natural Science Foundation of China (11005124 and 11275229), the Natural Science Foundation of Anhui Province (1208085QA05), and the National Fund for Scientific Research (FNRS) of Belgium.

K.-J. Zhao (✉) · Y.-G. Li
Department of Nuclear Science and Engineering
and Materials Science and Engineering,
Massachusetts Institute of Technology,
Cambridge, Massachusetts 02139, USA
e-mail: kzhao@mit.edu

Y.-G. Li
Key Laboratory for Materials Physics,
Institute of Solid State Physics,
Chinese Academy of Sciences, 230031 Hefei, China

L. Brassart
Institute of Mechanics, Materials and Civil Engineering,
Université catholique de Louvain,
Louvain-la-Neuve 1348, Belgium

Keywords Li-ion batteries · Si · Pressure-sensitive plasticity · Ratcheting.

1 Introduction

Li-ion batteries have attracted significant attention for applications in portable electronics, electric vehicles, stationary electricity storage, and load leveling of renewable energy sources [1, 2]. In the quest to develop high-energy-density Li-ion batteries, Si becomes one of the most promising anodes given its remarkable capability to absorb Li [3]. Compared to the conventional carbon-based anode in which every 6 carbon atoms can absorb 1 Li atom, each Si atom can host up to 4.4 Li atoms, making Si the anode material with the highest theoretical specific capacity. However, commercialization of Si is limited by the massive deformation and the consequent severe mechanical instability during the cyclic lithiation—upon reaching the theoretical capacity, the volume of Si swells more than 400% [4]. The intrinsic large deformation induces a field of stress in the electrodes, causing fracture of both active electrodes and conductive matrix, and resulting into the loss of conduction path of electrons [5–8]. Moreover, the drastic deformation poses a challenge on the chemical stability of Si electrodes. The chemical degradation of Si is mainly attributed to the dynamic formation of solid electrolyte interface (SEI) resulting from the side reactions of the electrode and the electrolyte [9]. The repeated swelling and shrinking of Si electrodes causes continuous breaking and re-forming of the SEI, which dynamically consumes the active materials and leads to irreversible capacity loss in the lithiation cycles. As a result, rapid capacity fade of Si electrodes often occur in the first few cycles.

The mechanical stability of Si anodes is largely enhanced with recent novel designs using nanostructured electrodes [10–19]. In these structures, the mechanical failure is mitigated by managing the deformation patterns through geometric restrictions and shape optimizations. For example, Takamura et al. [20] fabricated a Si thin film with thickness of 50 nm that maintains over a thousand cycles with-

out fracture. During lithiation, the large deformation of Si was accommodated by the surface morphological undulation, a type of roughening also observed in lithiation of Si nanowires [10]. Moreover, in a recent remarkable design, Wu et al. [21] manufactured Si anodes with hollow core-shell nanostructures, which enable the electrodes to maintain over six thousand cycles with little capacity fade. In such a nanostructure, a silicon oxide shell separates the electrolyte and Si, and encapsulates the deformation of Si within the hollow space in the interior of the structure. Direct contact between the electrode and the electrolyte is avoided, preventing the continual SEI shedding and re-forming. Similar designs based on the same concept have shown promise for Si to sustain hundreds of cycles [22, 23]. It is noteworthy that lithiation-induced plasticity plays a key role for Si to maintain long cycle life in the above designs. The surface undulation demonstrates a feature of plastic flow of Si thin film electrodes—the large deformation is accommodated by the morphological change and stresses are effectively relieved in the process. Also the core-shell structure takes advantage of the flowability of lithiated silicon to constrain the deformation in the interior hollow space. Meanwhile, since the stress at the interface between the core and the shell generated upon lithiation is upper-bounded by the yield strength of lithiated silicon, one can use a thin layer of oxide shell to restrict the deformation of Si core without fracture.

Lithiation-induced plasticity has been studied both experimentally and theoretically. Sethuraman et al. [24, 25] monitored the in-situ evolution of the stress field in a lithiation and delithiation cycle for an amorphous Si (a-Si) thin film electrode using the wafer curvature method. They showed that at the initial lithiation, the thin film behaves elastically and the stress increases linearly in the first stage. With further lithiation, the stress reaches compressive yield strength and inelastic flow sets in to accommodate the deformation. Upon delithiation, the compressive stress unloads elastically within a narrow range of Li composition, and then the stress reaches tensile yield strength. The hysteresis demonstrated in a lithiation and delithiation cycle clearly indicate plastic deformation of lithiated silicon. Such measurements were also preformed in other groups [26, 27]. Continuum models that account for the coupled diffusion of Li and large plastic deformation of electrodes have been developed recently [28–33]. Brassart and Suo [34, 35] further proposed a model of reactive flow that considers the concurrent nonequilibrium processes of Li insertion reaction and plastic flow of electrodes and generalizes the thermodynamic formulation of plasticity in an electrode under combined chemo-mechanical load. The structural evolution of amorphous Si during lithiation was studied using first-principles calculations [36–38]. Zhao et al. [38] investigated the microscopic mechanism of plasticity in lithiated silicon, and concluded that at the atomic scale the continuous bond breaking and re-forming assisted by Li insertion accommodates the large plastic deformation.

Experimental measurements of stress evolution in a Si thin film electrode exhibit asymmetry between the tensile and compressive stresses [24–27]. We show the schematic of typical experimental assessments of the stress evolution in Fig. 1a. Although the yield stresses during lithiation and delithiation both vary slightly with the state of charge, the magnitude of the compressive yield strength is higher than the tensile yield strength for a given Li composition. Haftbaradaran et al. [39] demonstrated that the compression-tensile asymmetry from lithiation to delithiation may cause accumulative and irreversible deformation of Si thin film electrodes—a mechanism of ratcheting. In Fig. 1b, we schematically reproduce the experimental observations. A continuous Si thin film with thickness of 250 nm is fractured after the first cycle [40]. Afterwards the size of the Si islands decreases and the gaps between the islands enlarge with cycles. This phenomenon was experimentally observed in Ref. [40] and reproduced numerically in Ref. [39]. We may speculate that similar accumulative deformation may occur in other geometries of electrodes such as nanoparticles. For a commercial battery that typically operates thousands of cycles, such irreversible deformation will pose a significant challenge of mechanical stability of electrodes in the long-term cycle life.

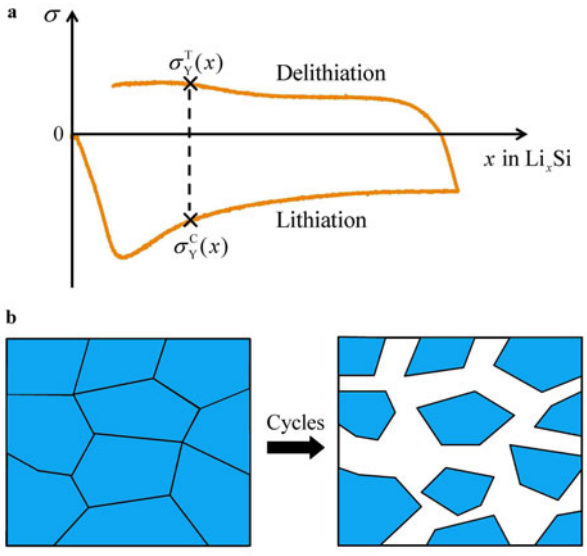

Fig. 1 a Schematic of the evolution of the biaxial stress in an a-Si thin film electrode during a lithiation and delithiation cycle. At a given lithium concentration, the compressive yield stress during lithiation and the tensile yield stress during delithiation are represented by σ_Y^C and σ_Y^T, respectively; **b** The asymmetry of the yield stresses from lithiation to delithiation leads to ratcheting of an a-Si thin film. The thin film is fractured after the first cycle. After a number of cycles, the size of the fractured islands decreases and the gaps between the islands enlarge. Such phenomenon was experimentally observed in Ref. [40], and was theoretically calculated in Ref. [39]

The compression-tension asymmetry in a-Si thin films may be attributed to the pressure-sensitive plasticity of lithiated silicon — the compressive hydrostatic stress suppresses the plastic flow of the amorphous structure thus enhances the yield strength. In this paper, we assess the dependence of the yield stress on the hydrostatic pressure by performing multi-axial load simulations using first-principles calculations. Three Li compositions, $Li_{0.25}Si$, $Li_{0.5}Si$, and LiSi, are considered. A linear dependence of the equivalent yield stress on the hydrostatic stress is demonstrated. We propose a yield criterion of lithiated silicon by including the effects of hydrostatic pressure and the lithiation reaction. We further examine the atomic mechanism of deformation of lithiated silicon by performing Voronoi polyhedra analysis and local coordination calculations. It is found that the localized bond switching at the loosely packed free-volume regions and cavitation accommodate the large plastic flow under mechanical load. A hydrostatic compressive stress confines the flow defects and thus effectively strengthens the amorphous structure, and vice versa.

2 Simulation method

We perform the first-principles calculations based on density functional theory (DFT) using the SIESTA code [41]. The amorphous Si structure contains 64 Si atoms with periodic boundary conditions. This size of supercell is consciously relatively small, because we aim to explore a large number of possible configurations of amorphous structures with various Li concentrations and a wide range of perturbation of equilibrium structures with applications of mechanical stresses. Our choice of supercell affords such studies at a reasonable balance of computational cost and accuracy. The atomic structures, system energy and stresses are calculated using a local-basis set of double-ς polarized atomic orbitals with an energy cutoff of 70 Ry (1 Ry = 13.606 eV). We use the Perdew–Burke–Enzerhof (PBE) exchange-correlation functional, norm-conserving pseudopotentials, and reciprocal-space mesh cutoff equivalent to a 10Å (1Å=0.1 nm) real-space period for the supercell. In energy optimization calculations, both the atomic coordinates and the supercell shape were fully relaxed. The energy optimization was considered complete when the magnitude of the force on each atom was smaller than 0.04 eV/Å.

The a-Si structure employed here was generated by quenching the liquid phase with explicit molecular dynamics using the environment dependent interatomic potential (EDIP) for Si, as described in more detail in our previous work [42, 43]. At each Li composition, we place Li atoms at energetically favorable positions in the a-Si network. We have identified 32 unique lowest-energy positions for a Li atom insertion into the a-Si network [38, 44]. In Li composition $Li_{0.25}Si$, the lithium atoms are located at the most energetically favorable sites out of the 32 lowest-energy positions. Full occupancy of all the 32 sites corresponds to the Li composition $Li_{0.5}Si$. For LiSi, we examine the local Li coordination neighbors of each Si atom and place further Li atoms in addition to the 32 sites around the Si atoms that have the lowest number of Li neighbors [26]. Here we focus on the static and equilibrium properties of lithiated silicon. Kinetic effects, such as the long range process of Li diffusion in Si, are not considered. Thus, in the modeling of deformation and stress, we assume the diffusion is fast enough to allow for a uniform distribution of Li.

In the simulation of material response under mechanical load, we prescribe a given stress level along each direction of the structure, and measure the nominal strain after full relaxation. To model the multi-axial load, we first apply a given hydrostatic pressure to a Li composition structure, and relax the structure to obtain the state of minimized energy. The relaxed configuration is taken as the reference state. Then we maintain the stresses at the y- and z-direction at the initial value, and increase the stress along the x-direction until it reaches the tensile strength of the structure before it is fractured. At this peak stress, the structure is stretched mostly and plastic flow is evidenced by drastic bond breaking and re-forming. It should be noted that rare local bond switching also occur at lower level of applied stress which indicates local atomic rearrangement. For clarification of the definition of the yield stress, we take the peak stress that the structure can sustain as the yield strength of the material.

We rely on the Voronoi polyhedra analysis to investigate the structural characteristics of amorphous lithiated silicon. The Voronoi analysis is performed to determine the surrounding Voronoi polyhedron (the space closer to a given atom than to any others) for each atom, using the minimum image convention and setting a cutoff beyond which atoms are assumed not coordinated [45]. The vertices of each Voronoi polyhedron can be found by intersecting any three perpendicular surfaces between the chosen atom and its neighbors. Then the volume of each polyhedron is calculated by summing the sub-volumes that equal to one-third of the product of the surface area and the length of the vertical line from the atoms.

3 Results and discussion

The stress–strain response curves of LiSi under different hydrostatic stresses are shown in Fig. 2a. Each curve represents tension along the x-direction starting from a different state of hydrostatic tension or compression. During tension, the stresses along the y- and z-direction are maintained at their initial value. The considered initial hydrostatic stresses range linearly from −3 to 3 GPa, as indicated in the color map. We represent the stress–strain curves as the evolution of the deviatoric stress as a function of applied strain along the x-direction, where the relaxed structure under a pure hydrostatic tension or compression is taken as the reference state. The deviatoric stress is defined as $s_{ij} = \sigma_{ij} - \sigma_{\mathrm{m}}\delta_{ij}$, where σ_{m} is the hydrostatic stress and δ_{ij} is the Kronecker delta. For each curve, the highest stress level represents the strength beyond which the structure is fractured. Here we

adopt the highest stress level as a measure of yield stress. The solid symbol curves represent the loading paths, and the open symbol curves represent the unloading paths. It is evident that substantial plastic deformation occurs in all the simulation cases. The network can be stretched by 20% – 40% without fracture, and large permanent deformation remains after unloading. The dependence of the deviatoric yield stress on the hydrostatic stress is summarized in Fig. 2b, for the three different Li compositions $Li_{0.25}Si$, $Li_{0.5}Si$, and LiSi, respectively. The solid symbols represent the simulation results, and the lines connecting the data are guide for the eye. Obviously, the deviatoric yield stress of lithiated silicon strongly depends on the hydrostatic stress. The magnitude of the deviatoric yield stress varies by factor of three within the range of the hydrostatic stresses considered. A positive hydrostatic stress makes flow easier, while a negative hydrostatic stress retards it. Such dependence may lead to the compression-tension yield stress asymmetry as observed in a-Si thin film electrodes upon a lithiation and delithiation cycle. Figure 2b also shows that the yield strength decreases with increasing Li composition. This softening effect was previously reported [26] and is attributed to the increase of Si coordination defects with Li concentration.

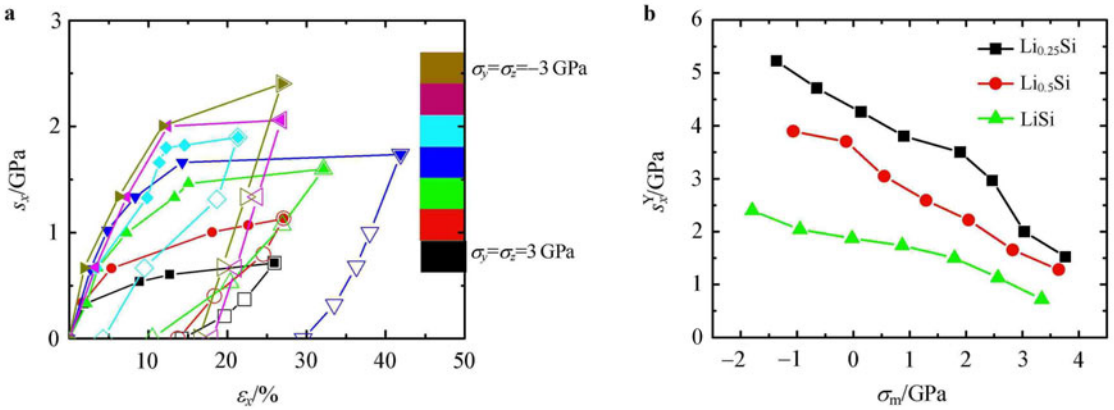

Fig. 2 **a** The stress–strain response of amorphous LiSi under multi-axial load with different hydrostatic stresses. To decouple the effect of pressure, the material response is represented by the evolution of the deviatoric stress as a function of applied strain along the x-direction. The solid-symbol lines represent the loading path; the open-symbol lines represent the unloading path; **b** Dependence of the deviatoric yield stress on the hydrostatic stress, for the three different lithiation phases $Li_{0.25}Si$, $Li_{0.5}Si$, and LiSi, respectively. The simulation results are represented by the solid symbols. The lines connecting the data are guide for the eye

A general yield criterion valid under arbitrary loading conditions can be derived from the simulation results by plotting the equivalent stress at yielding, $\sigma_e^Y = \sqrt{\frac{3}{2}s_{ij}^Y s_{ij}^Y}$, as a function of the hydrostatic stress (Fig. 3). The solid symbols represent the simulation results, and the dashed lines are the linear fitting of the yield conditions of the different lithiated phases. A linear dependence of the equivalent stress on the hydrostatic stress at yielding reasonably captures the relationship over the range of hydrostatic stress considered here. Such linear function may be recast into a form similar to the Drucker–Prager yield condition [46, 47]

$$\sigma_e^Y + A\sigma_m = B, \tag{1}$$

where A and B are the fitting parameters. Using the simulation data in Fig. 3, we obtain the parameters A = 1.03, 0.88, 0.44, and B = 6.56, 5.01, 2.83 GPa, for $Li_{0.25}Si$, $Li_{0.5}Si$, LiSi, respectively. According to the Drucker–Prager yield criterion, the parameter B represents the yield stress under pure shear loading, and the ratio B/A is the yield stress under pure hydrostatic tension.

The yield criterion (1) can be used to investigate yielding in a thin film electrode upon lithiation and delithiation, as depicted in Fig. 1. Assuming a homogeneous, biaxial state of stress within the film, the mean stress is $\sigma_m = 2\sigma_b/3$ and the equivalent stress is $\sigma_e = |\sigma_b|$, with σ_b the biaxial stress, corresponding to a triaxiality ratio $\sigma_m/\sigma_e = \pm 2/3$. From Eq. (1), one can easily derive the yield stress in tension and compression as

$$\sigma_b^{Y,T} = \frac{3B}{3+2A}, \qquad \sigma_b^{Y,C} = \frac{3B}{3-2A}. \tag{2}$$

With the fitting parameters obtained from Fig. 3, Eq. (2) gives $\sigma_b^{Y,T}$ = 3.9, 3.2, 2.2 GPa, and $\sigma_b^{Y,C}$ = 20.9, 12.1, 4.0 GPa for $Li_{0.25}Si$, $Li_{0.5}Si$, LiSi, respectively. These estimates are significantly higher than experimentally measured values of yield stresses in thin-film electrodes [24–27], which typically range between 0.5 and 1.5 GPa, depending on the lithium content. In particular, the magnitudes of the yield stresses in compression as obtained from the linear fitting are unrealistically high. Most probably, this indicates that the linear fitting is not valid for low, negative triaxiality ratios (in the negative range). Additional numerical results are needed to confirm this hypothesis. On the other hand, the

discrepancy between numerical and experimentally observed yield stress values under biaxial tension can be attributed lithiation-assisted flow: the lithiation reaction enables flow of lithiated silicon at a lower stress than that needed for flow under pure mechanical loading. This proposed mechanism is elaborated in details in a previous work [26].

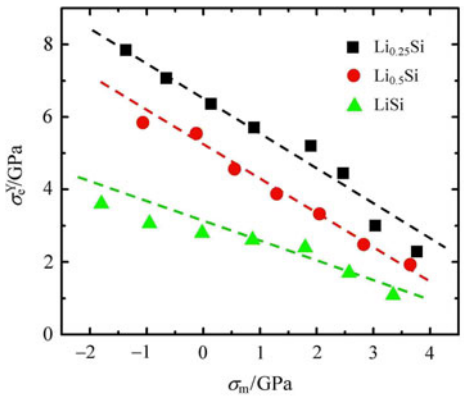

Fig. 3 The yield condition of lithiated silicon under mechanical load is represented by the dependence of the equivalent yield stress on the hydrostatic pressure. The dashed lines are the linear fitting of the yield conditions of the different lithiated phases

To account for lithiation-assisted flow, we extend the yield condition (1) of lithiated silicon following a recently proposed theory of reactive flow in solids [35]. According to this theory, inelastic deformation of lithiated silicon and the lithiation reaction are regarded as concurrent nonequilibrium processes. The Li insertion is driven by the change of free energy associated with the chemical reaction xLi+Si=Li$_x$Si [48]. Let ΔG_r be the change of free energy when both the stress and applied voltage vanish. The driving force is modified when the lithiated silicon is stressed. Associated with inserting one Li into Si, the stress does work $-\Omega\sigma_\mathrm{m}$, where Ω is the volume change of Si caused by inserting one Li. By neglecting the effect of the external electric field, the driving force for the Li insertion can be written as

$$\Delta G = \Delta G_\mathrm{r} - \Omega\sigma_\mathrm{m}. \tag{3}$$

The free energy of reaction ΔG_r takes a negative value during Li insertion. A compressive hydrostatic stress retards Li insertion, and a tensile mean stress promotes Li insertion. In our sign convention, a negative ΔG drives lithiation, and a positive ΔG drives delithiation. We may define the driving force for the lithiation reaction in the dimension of stress as $\chi = \Delta G_\mathrm{r}/\Omega - \sigma_\mathrm{m}$. On the other hand, in the absence of chemical reaction, flow of lithiated silicon is driven by a combination of the hydrostatic stress and deviatoric stress, according to the results shown in Fig. 3. When lithiated silicon is subject to concurrent mechanical and chemical loading, the lithiation reaction can decrease the stress needed for flow. We formulate the chemomechanical yield condition of reactive flow of lithiated silicon by placing the driving force for reaction and flow on the same footing. A straightforward generalization of the Drucker–Prager yield condition (1) may be written

$$\sqrt{\frac{3}{2}s_{ij}s_{ij}} + p\sigma_\mathrm{m} + q|\chi| = \sigma_\mathrm{Y}, \tag{4}$$

where σ_Y is the yield strength of lithiated silicon under pure deviatoric stress, and p, q are dimensionless, positive constants indicating the relative contributions of the hydrostatic stress and chemical driving force to the scalar measure of the driving force of reactive flow of lithiated silicon. In general, σ_Y, p, and q all depend on the Li concentration. Under pure mechanical loading, the parameters σ_Y and p coincide with the parameters B and A in Eq. (1). The parameter q may in principle be obtained through a stress-free lithiation experiment, see Ref. [34]. Note that yielding depends on the sign of the hydrostatic stress, while it is independent of the sign of the chemical driving force. In other words, lithium insertion or extraction reactions both promote flow. Evidently, the particular form of the yield condition (1) is not the only possible one. Validation and refinement of condition (4) need to be supported by experiments.

We now examine the atomic mechanism of plastic deformation of amorphous lithiated silicon subject to the yield stress. A representative deformation pattern of $Li_{0.5}Si$ under uniaxial tensile yield stress is shown in Fig. 4. Figure 4a shows the initial configuration of $Li_{0.5}Si$ without stresses, in which the blue spheres represent the Si atoms, and the red spheres represent the Li atoms. Compared with the pristine coordination-free Si network, the presence of Li breaks certain numbers of Si–Si bonds but a well-defined network still exists and spans the size of the supercell. Close inspection shows that Li atoms distribute inhomogeneously, leaving certain Si bonds more disturbed than others. The deformation pattern under the uniaxial tensile yield stress is shown in Fig. 4b. In this configuration, the nominal strain reaches about 40%. However, such large deformation is mainly accommodated by local bond switching and consequent generation of cavitation, as marked by the black circle. Such localized deformation mechanism may share the same feature of shear transformation in glassy materials [49–51]. It is generally perceived that amorphous network consists of tightly bonded clusters, which form the backbone of the structure, and loosely bonded free-volume regions, which act as flow defects and behave liquid-likely responding to the external mechanical load [52]. The flow defects may be caged by the tightly bonded surroundings, which constitute the basic topological feature of the atomic structure. Under mechanical load, the deformation is mainly localized in the loosely packed regions (weak regions) while the backbone (strong regions) behaves elastically. Such deformation mechanism is evidenced in lithiated silicon, Fig. 4b.

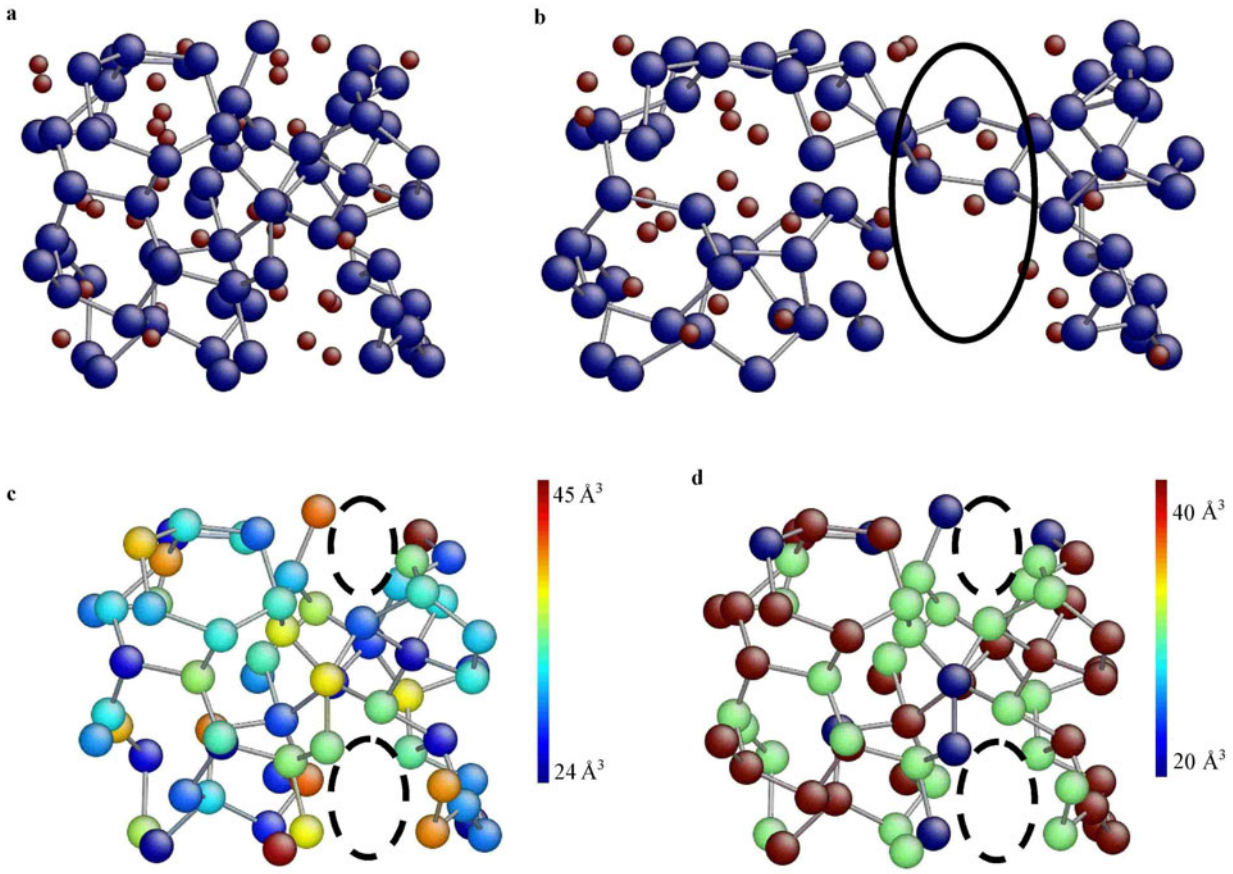

Fig. 4 The atomistic deformation mechanism of $Li_{0.5}Si$ under the uniaxial tensile yield stress. **a** The atomic structure of $Li_{0.5}Si$ without stresses. Blue spheres represent Si atoms, and red spheres represent Li atoms; **b** The atomic configuration after applying the uniaxial yield stress. The deformation is mainly mediated by the local bond switching and cavitation, as marked by the black circle; **c** Si atoms are color-coded according to the atomic Voronoi volume. Atoms with larger Voronoi volumes, as highlighted by the dashed circles, represent local loosely packed regions where the deformation is mainly accommodated; **d** Si atoms are color-coded according to the Si–Si coordination. The less bonded regimes, corresponding to the large free-volume zones, represent the flow defects of lithiated silicon under mechanical loading

To quantify the inhomogeneity of the local strength, we perform the Voronoi polyhedra analysis and atomic coordination calculations. It should be noted that, during lithiation of Si, the covalent Si–Si bonds are broken by the presence of neighboring Li atoms, and Si–Li atoms form a weak bond of ionic character, with charge depletion of the Li atom and charge accumulation closer to the Si atom [38]. Thus, we believe that the remaining Si–Si bonds network in lithiated silicon forms the skeleton of the structure and mainly determines the mechanical behavior of the material. As such, in the Voronoi analysis, we focus on the Si atoms and neglect the presence of the Li atoms. In Fig. 4c, Si atoms are color-coded according to the atomic Voronoi volumes; red color represents large Voronoi volumes and blue color represents small ones. We highlight the atoms with large free volume by the dashed circles. It is clearly seen that the loosely packed free-volume regions percolated in the network. Upon applying a field of stress, these regions become active in deformation and act as flow defects that accommodate the most deformation by atomic bond switching and cavitation. The strength of the Si network is also indicated by the local Si coordination number. To determine a physically meaningful Si coordination, we define two Si atoms to be bonded if their distance is within 15% of the covalent bond length in bulk c–Si 2.37 Å, which corresponds to a largest distance of 2.72 Å. In Fig. 4d, Si atoms are color-coded according to the coordination number. It is seen that the less bonded regime corresponds to the large free-volume regions in Fig. 4c. Combined with Fig. 4b, we conclude that the large plastic flow of lithiated silicon is mainly mediated by the localize deformation in the weak regions of flow defects, while the strength of the structure is determined by the neighboring backbone

of tightly bonded Si atoms.

To investigate the effect of the hydrostatic pressure on the yield strength of lithiated silicon, we take a representative composition $Li_{0.5}Si$, and calculate the Voronoi volumes of Si and Li atoms at various hydrostatic stresses. To have a better statistics, we consider five different configurations and each configuration is subject to the hydrostatic stresses $\sigma_m = -2, 0, 2$ GPa, respectively. In calculating the Voronoi volume of Si atoms, again we have ignored the presence of the neighboring Li atoms. Figure 5a shows the distribution of the Voronoi volume of Si atoms. The solid symbols represent the calculated results, with an interval of 2 Å^3 for each point. The smooth curves are the fitting curves using the B-spline numerical method [53]. It is evident that, by increasing the hydrostatic stress from compression to tension, more flow defects, as indicated by the loosely packed free volumes at the tail of the curves, are generated. These flow defects promote the plastic deformation of lithiated silicon at a lower level of stress. Moreover, as the hydrostatic tension increases, the peak of the atomic volume is shifted towards a larger value, and the height of the peak decreases. Such characteristics lead to an overall softer behavior of lithiated silicon under tensile stresses. In addition, we plot the distribution of the Voronoi volume of Li atoms in Fig. 5b by accounting for all the atoms in the structure. Each point represents a value with an interval of 1 Å^3. Li atoms are relatively mobile in the amorphous structure given the weak bonding between the Si and Li atoms. Such high mobility allows for continuous Si–Si bond breaking and re-forming assisted by Li atoms during deformation. Thus, Li atoms act like "lubricant" in a "rigid" Si network. From Fig. 5b, it is clearly shown that the atomic volume of the Li atoms increases by applying a hydrostatic tensile stress. The larger free volume leads to a higher mobility of Li atoms, and further facilitates the flowability of the amorphous network.

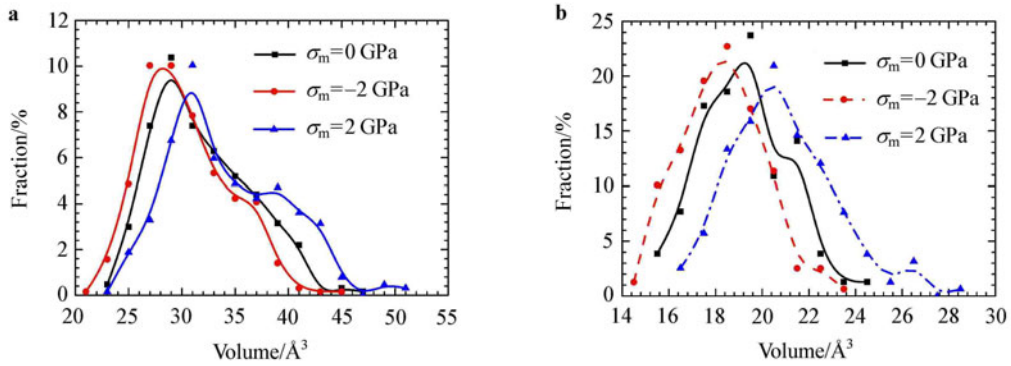

Fig. 5 The distribution of Voronoi volume of **a** Si atoms, and **b** Li atoms, in $Li_{0.5}Si$ at various hydrostatic pressures. The atomic volumes are obtained from five different configurations. The solid symbols represent the calculation data, with an interval of 2 Å^3 (1 Å^3) for Si (Li) atoms for each point. The smooth lines are the fitting curves using the B-spline numerical method. In calculating the Voronoi volume of Si atoms, the presence of Li atoms is ignored based on the assumption that the mechanical behavior of lithiated silicon is mainly dominated by the Si–Si bonds

4 Conclusions

We study the plasticity of lithiated silicon under multi-axial mechanical load using first-principles calculations. The linear pressure-dependent equivalent yield stress of various Li compositions is illustrated. We propose a yield criterion that includes the effects of the hydrostatic stress and chemical reactions by formulating a yield condition as a function of the mechanical driving force for flow and the chemo-mechanical driving force for reactions. We examine the atomic mechanism of plasticity of amorphous lithiated silicon using the Voronoi polyhedra analysis and local coordination calculations. The large plastic deformation is mainly mediated by the localized bond switching in the loosely packed free-volume regions and subsequent cavitation. A hydrostatic compressive stress confines the flow defects and effectively strengthens the material, while a hydrostatic tensile stress generates more flow defects and promotes the plasticity of lithiated silicon at a lower level of stress.

Acknowledgements The author K.-Z. Zhao acknowledges helpful discussions with Ju Li at MIT, Joost Vlassak, and Matt Pharr at Harvard. Time on the Harvard School of Engineering and Applied Sciences HPC compute cluster and support by the SEAS Academic Computing team are gratefully acknowledged. The authors have also used the Extreme Science and Engineering Discovery Environment (XSEDE), supported by NSF of US (TG-DMR130025 and TG-DMR130038).

References

1 Armand, M., Tarascon, J.M.: Building better batteries. Nature **451**, 652–657 (2008)
2 Choi, N.S., Chen, Z.H., Freunberger, S.A., et al.: Challenges

facing lithium batteries and electrical double-layer capacitors. Angew. Chem. Int. Edit. **51**, 9994–10024 (2012)
3 Kasavajjula, U., Wang, C.S., Appleby, A.J.: Nano- and bulk-silicon-based insertion anodes for lithium-ion secondary cells. J. Power Sources **163**, 1003–1039 (2007)
4 Zhang, W.J.: A review of the electrochemical performance of alloy anodes for lithium-ion batteries. J. Power Sources **196**, 13–24 (2011)
5 Huggins, R.A., Nix, W.D.: Decrepitation model for capacity loss during cycling of alloys in rechargeable electrochemical systems. Ionics **6**, 57–64 (2000)
6 Zhao, K.J., Pharr, M., Vlassak, J.J., et al.: Fracture of electrodes in lithium-ion batteries caused by fast charging. J Appl. Phys. **108**, 073517 (2010)
7 Zhao, K.J., Pharr, M., Hartle, L., et al.: Fracture and debonding in lithium-ion batteries with electrodes of hollow core-shell nanostructures. J. Power Sources **218**, 6–14 (2012)
8 Pharr, M., Zhao, K.J., Wang, X.W., et al.: Kinetics of initial lithiation of crystalline silicon electrodes of lithium-ion batteries. Nano Lett. **12**, 5039–5047 (2012)
9 Choi, N.S., Yao, Y., Cui, Y., et al.: One dimensional Si/Sn - based nanowires and nanotubes for lithium-ion energy storage materials. J. Mat. Chem. **21**, 9825–9840 (2011)
10 Chan, C.K., Peng, H.L., Liu, G., et al.: High-performance lithium battery anodes using silicon nanowires. Nat. Nanotech. **3**, 31–35 (2008)
11 Cui, L.F., Hu, L.B., Choi, J.W., et al.: Light-weight free-standing carbon nanotube-silicon films for anodes of lithium ion batteries. Acs. Nano **4**, 3671–3678 (2010)
12 Haftbaradaran, H., Xiao, X.C., Verbrugge, M.W., et al.: Method to deduce the critical size for interfacial delamination of patterned electrode structures and application to lithiation of thin-film silicon islands. J. Power Sources **206**, 357–366 (2012)
13 Kim, H., Han, B., Choo, J., et al.: Three-dimensional porous silicon particles for use in high-performance lithium secondary batteries. Angew. Chem. Int. Edit. **47**, 10151–10154 (2008)
14 Krishnan, R., Lu, T.M., Koratkar, N.: Functionally strain-graded nanoscoops for high power Li-ion battery anodes. Nano Lett. **11**, 377–384 (2011)
15 Magasinski, A., Dixon, P., Hertzberg, B., et al.: High-performance lithium-ion anodes using a hierarchical bottom-up approach. Nat. Mater. **9**, 353–358 (2010)
16 Wang, J.W., Liu, X.H., Zhao, K.J., et al.: Sandwich-lithiation and longitudinal crack in amorphous silicon coated on carbon nanofibers. Acs. Nano **6**, 9158–9167 (2012)
17 Yao, Y., McDowell, M.T., Ryu, I., et al.: Interconnected silicon hollow nanospheres for lithium-Ion battery anodes with long cycle life. Nano Lett. **11**, 2949–2954 (2011)
18 Yu, C.J., Li, X., Ma, T., et al.: Silicon thin films as anodes for high-performance lithium-ion batteries with effective stress relaxation. Adv. Energy Mater. **2**, 68–73 (2012)
19 Zhang, S.C., Du, Z.J., Lin, R.X., et al.: Nickel nanocone-array supported silicon anode for high-performance lithium-ion batteries. Adv. Mater. **22**, 5378–5382 (2010)
20 Takamura, T., Ohara, S., Uehara, M., et al.: A vacuum deposited Si film having a Li extraction capacity over 2 000 mA·h/g with a long cycle life. J. Power Sources **129**, 96–100 (2004)
21 Wu, H., Chan, G., Choi, J.W., et al.: Stable cycling of double-walled silicon nanotube battery anodes through solid-electrolyte interphase control. Nat. Nanotech. **7**, 309–314 (2012)
22 Wu, H., Zheng, G.Y., Liu, N.A., et al.: Engineering empty space between Si nanoparticles for lithium-ion battery anodes. Nano Lett. **12**, 904–909 (2012)
23 Hwang, T.H., Lee, Y.M., Kong, B.S., et al.: Electrospun core-shell fibers for robust silicon nanoparticle-based lithium ion battery anodes. Nano Lett. **12**, 802–807 (2012)
24 Sethuraman, V.A., Chon, M.J., Shimshak, M., et al.: In situ measurements of stress evolution in silicon thin films during electrochemical lithiation and delithiation. J. Power Sources **195**, 5062–5066 (2010)
25 Sethuraman, V.A, Chon, M.J., Shimshak, M., et al.:In situ measurement of biaxial modulus of Si anode for Li-ion batteries. Electrochem. Commun. **12**, 1614–1617 (2010)
26 Zhao, K.J., Tritsaris, G.A., Pharr, M., et al.: Reactive flow in silicon electrodes assisted by the insertion of lithium. Nano Lett. **12**, 4397–4403 (2012)
27 Soni, S.K., Sheldon, B.W., Xiao, X.C., et al.: Thickness effects on the lithiation of amorphous silicon thin films. Scripta Mater. **64**, 307–310 (2010)
28 Anand, L.: A Cahn-Hilliard-type theory for species diffusion coupled with large elastic-plastic deformations. J. Mech. Phys. Solids **60**, 1983–2002 (2012)
29 Cui, Z.W., Gao, F., Qu, J.M.: A finite deformation stress-dependent chemical potential and its applications to lithium ion batteries. J. Mech. Phys. Solids **60**, 1280–1295 (2012)
30 Bower, A.F., Guduru, P.R., Sethuraman, V.A.: A finite strain model of stress, diffusion, plastic flow, and electrochemical reactions in a lithium-ion half-cell. J. Mech. Phys. Solids **59**, 804–828 (2011)
31 Zhao, K.J., Pharr, M., Vlassak, J.J., et al.: Inelastic hosts as electrodes for high-capacity lithium-ion batteries. J. Appl. Phys. **109**, 016110 (2011)
32 Brassart, L., Zhao, K.J., Suo, Z.G.: Cyclic plasticity and shake-down in high-capacity electrodes of lithium-ion batteries. Int. J. Solids Struct. **50**, 1120–1129 (2013)
33 Zhao, K.J., Pharr, M., Cai, S. Q., et al.: Large plastic deformation in high-capacity lithium-ion batteries caused by charge and discharge. J. Am. Ceram. Soc. **94**, S226–S235 (2011)
34 Brassart, L., Suo, Z.G.: Reactive flow in large-deformation electrodes of lithium-ion batteries. Int. J. Appl. Mech. **4**, 1250023 (2012)
35 Brassart, L., Suo, Z.G.: Reactive flow in solids. J. Mech. Phys. Solids **61**, 61–77 (2013)
36 Chevrier V.L., Dahn, J.R.: First principles model of amorphous silicon lithiation. J. Electrochem. Soc. **156**, A454–A458 (2009)
37 Huang, S., Zhu, T.: Atomistic mechanisms of lithium insertion in amorphous silicon. J. Power Sources **196**, 3664–3668 (2011)
38 Zhao, K.J., Wang, W. L., Gregoire, J., et al.: Lithium-assisted plastic deformation of silicon electrodes in lithium-ion batteries: A first-principles theoretical study. Nano Lett. **11**, 2962–2967 (2011)
39 Haftbaradaran, H., Gao, H.J.: Ratcheting of silicon island electrodes on substrate due to cyclic intercalation. Appl. Phys. Lett. **100**, 121907 (2012)
40 Maranchi, J.P., Hepp, A.F., Evans, A.G., et al.: Interfacial properties of the a-Si/Cu: Active-inactive thin-film anode system for

lithium-ion batteries. J. Electrochem. Soc. **153**, A1246–A1253 (2006)
41 Soler, J.M., Artacho, E., Gale, J.D., et al.: The SIESTA method for ab initio order-N materials simulation. J. Phys.-Condes. Matter **14**, 2745–2779 (2002)
42 Bazant, M.Z., Kaxiras, E., Justo, J. F.: Environment-dependent interatomic potential for bulk silicon. Phys. Rev. B **56**, 8542–8552 (1997)
43 Mo, Y., Bazant, M. Z., Kaxiras, E.: Sulfur point defects in crystalline and amorphous silicon. Phys. Rev. B **70**, 205210 (2004)
44 Tritsaris G.A., Zhao, K.J., Okeke, O.U., et al.: Diffusion of lithium in bulk amorphous silicon: A theoretical study. J. Phys. Chem. C **116**, 22212–22216 (2012)
45 Allen, M.P., Tildesley, D.J.: Computer Simulation of Liquids. Clarendon Press, Oxford (1987)
46 Drucker, D.C., Prager, W.: Soil mechanics and plastic analysis for limit design. Q. Appl. Math. **10**, 157–165 (1952)
47 Jin, M.Z., Chen, C.Q., Lu, T.J.: The mechanical behavior of porous metal fiber sintered sheets. J. Mech. Phys. Solids **61**, 161–174 (2013)
48 Zhao, K.J., Pharr, M., Wan, Q., et al.: Concurrent reaction and plasticity during initial lithiation of crystalline silicon in lithium-ion batteries. J. Electrochem. Soc. **159**, A238–A243 (2012)
49 Argon, A.S., Demkowicz, M.J.: What can plasticity of amorphous silicon tell us about plasticity of metallic glasses? Metall. Mater. Trans. A-Phys. Metall. Mater. Sci. **39**, 1762–1778 (2008)
50 Schuh C.A., Lund, A.C.: Atomistic basis for the plastic yield criterion of metallic glass. Nature **2**, 449–452 (2003)
51 Gao, Y.F., Wang, L., Bei, H., et al.: On the shear-band direction in metallic glasses. Acta Mater. **59**, 4159–4167 (2011)
52 Ye, J.C., Lu, J., Liu, C.T., et al.: Atomistic free-volume zones and inelastic deformation of metallic glasses. Nat. Mater. **9**, 619–623 (2011)
53 Boor C.D.: A Practical Guide to Splines. Springer-Verlag, New York, 113–114 (1978)